Sensitivity of Global Tropical Climate to Land Surface Processes: Mean State and Interannual Variability

Hsi-Yen Ma

Program for Climate Model Diagnosis and Intercomparison, Lawrence Livermore National Laboratory,
Livermore, California

Heng Xiao

Atmospheric Sciences and Global Change Division, Pacific North National Laboratory, Richland, Washington

C. Roberto Mechoso

Department of Atmospheric and Oceanic Sciences, University of California, Los Angeles, Los Angeles, California

Yongkang Xue

Department of Atmospheric and Oceanic Sciences, and Department of Geography, University of California,
Los Angeles, Los Angeles, California

ABSTRACT

This study examines the sensitivity of the global climate to land surface processes (LSP) using an atmospheric general circulation model both uncoupled (with prescribed SSTs) and coupled to an oceanic general circulation model. The emphasis is on the interactive soil moisture and vegetation biophysical processes, which have first-order influence on the surface energy and water budgets. The sensitivity to those processes is represented by the differences between model simulations, in which two land surface schemes are considered: 1) a simple land scheme that specifies surface albedo and soil moisture availability and 2) the Simplified Simple Biosphere Model (SSiB), which allows for consideration of interactive soil moisture and vegetation biophysical process. Observational datasets are also employed to assess the extent to which results are realistic.

The mean state sensitivity to different LSP is stronger in the coupled mode, especially in the tropical Pacific. Furthermore, the seasonal cycle of SSTs in the equatorial Pacific, as well as the ENSO frequency, amplitude, and locking to the seasonal cycle of SSTs, is significantly modified and more realistic with SSiB. This outstanding sensitivity of the atmosphere–ocean system develops through changes in the intensity of equatorial Pacific trades modified by convection over land. The results further demonstrate that the direct impact of land–atmosphere interactions on the tropical climate is modified by feedbacks associated with perturbed oceanic conditions ("indirect effect" of LSP). The magnitude of such an indirect effect is strong enough to suggest that comprehensive studies on the importance of LSP on the global climate have to be made in a system that allows for atmosphere–ocean interactions.

1. Introduction

Future projections of global and regional precipitation and clouds over land by climate models for different climate change scenarios in the Intergovernmental Panel on Climate Change (IPCC) Fourth Assessment Report (AR4; Solomon et al. 2007) show large intermodel spread both in sign and in magnitude. The different representation of land surface processes (LSP; involving biogeophysics and biogeochemistry) in these climate models, and/or the associated sensitivity to changes in land surface conditions, is one of the principal contributors to the spread and uncertainty (e.g., Henderson-Sellers et al. 2003; Boone et al. 2004; Koster et al. 2004, 2006; Seneviratne et al. 2006; Bader et al. 2008; Wei and Dirmeyer 2010;

Wei et al. 2010; Xue et al. 2006, 2010). Land surface processes affect the exchanges of momentum, radiation, sensible and latent heat fluxes, and trace gases and aerosols between land and the overlying atmosphere through the planetary boundary layer (PBL). These exchanges influence the large-scale flow, precipitation, and cloudiness on both short- and long-term time scales. The problem posed by the sensitivity of climate to land surface processes, therefore, involves multiscale, nonlinear interactions between different physical processes.

A perusal of the scientific literature on the sensitivity of climate to land surface processes portrays an extremely active field of research. For example, atmospheric general circulation model (AGCM) simulations with and without land–atmosphere interactions performed by Delworth and Manabe (1988, 1989) demonstrated that the interactive treatment of soil moisture allows for larger variations in space and time of surface energy fluxes, thereby increasing the variance of surface air temperature. A series of AGCM ensemble simulations coordinated by the Global Land–Atmosphere Coupling Experiment (GLACE; Koster et al. 2004, 2006) identified continental regions of strong coupling between soil moisture and precipitation during the boreal summer (June–August). The existence of such "hot spots" suggests that the proper initialization of soil moisture may improve the skill in prediction of regional precipitation during the warm season. Xue et al. (2010) examined the importance of vegetation biophysical processes (VBP)—in addition to interactive soil moisture—in simulations by the National Centers for Environmental Prediction (NCEP) and University of California, Los Angeles (UCLA) AGCMs. The Xue et al. (2010) study identified regions of strong climate–VBP interactions over the global continents, especially in West Africa, South Asia, East Asia, and South America. The seasons of strongest impact were found to depend upon region. In general, the larger impacts occur during the monsoon seasons, when local precipitation can be as large as 40% of the annual mean.

Recent studies report systematic comparisons of AGCM simulations performed with several land surface schemes. Wei et al. (2010) examined the impacts of doubled CO_2 on the simulated surface warming using a single AGCM coupled to three different land schemes. They found the choice of land scheme to significantly affect the spatial distribution and amplitude of the simulated warming over land. Wei and Dirmeyer (2010) performed similar experiments using two AGCMs coupled to three land surface schemes. They found uncertainties in global precipitation variability, predictability, and land–atmosphere coupling strength to depend primarily upon the AGCM, with the land surface schemes providing a secondary

contribution. Projections of regional climate change by an AGCM, therefore, can significantly depend on the treatment of land surface processes.

A few AGCM studies have discussed the possible impacts of land surface processes on the atmospheric circulation over ocean. Using the European Centre for Medium-Range Weather Forecasts (ECMWF) AGCM coupled to an equatorial Pacific-only ocean model, Barnett et al. (1989) showed that a weak South Asian monsoon is associated with a colder land surface over Eurasia (where snow cover is heavier), as well as with weaker surface wind stress and changed heat fluxes over the tropical Pacific. Based on simulations by several AGCMs, Meehl (1994) concluded that a weaker South Asia monsoon is associated with decreased land–sea contrasts as well as wetter and colder land surface condition. The latter conditions result in weak easterly trades over the Pacific.

All the studies mentioned above prescribed sea surface temperatures (SSTs) and therefore bypassed the "indirect effects" of land surface processes due to changes in ocean–atmosphere interactions. Analyses with coupled ocean–atmosphere models of different complexity, however, have hinted to the importance of properly capturing those indirect effects for the better simulation of climate in regions of strong air–land interaction, such as those in which major monsoons develop (e.g., Wang et al. 2005; Wu et al. 2006; Misra 2008). Fu and Wang (2003) used an atmosphere–ocean (Pacific only)–land coupled model of intermediate complexity to examine the important roles of air–sea coupling and adjacent continental monsoons on the annual mean and seasonal cycle of the equatorial Pacific SST. They argued that the more successful simulation of convection associated with the Asian–Australian monsoons results in improved mean SST in the western Pacific through enhancements in the strength of the trades and in a more correct semiannual cycle of surface wind speed and SST in the equatorial western Pacific. These corresponding effects, however, are small in the eastern Pacific SST. In contrast, Fu and Wang (2003) argued that convection associated with the South American monsoon does not affect the mean SST but exerts a strong influence on the annual variations of the southeast trades and SST in the eastern Pacific.

The land-cover change is an important land surface process and a few studies have considered the impact of changing land surface conditions on the climate over the oceans (e.g., Zeng et al. 1996; Zeng and Neelin 1999; Hu et al. 2004; Swann et al. 2011). Zeng et al. (1996) investigated the impact of Amazon deforestation on the tropical SST using an intermediate-complexity model. Their results indicated that, in the Atlantic basin, the

impact of deforestation-included warm SST anomalies in the west and cold SST anomalies in the east resulted in a decrease of the basinwide zonal SST gradient by 1°C along the equator. Hu et al. (2004) used a coupled ocean–atmosphere GCM (CGCM) to assess the sensitivity of El Niño–Southern Oscillation (ENSO) to soil moisture. They compared a control simulation with prognostic soil moisture and a sensitivity experiment with specified deep soil moisture. In their experiment of specified soil moisture, a net energy sink over land causes a cooling of tropical land. The cooling is connected to changes in the mean state of the coupled system, including a shift in the land–sea partitioning of precipitation toward the oceans, a more westerly wind stress over the tropical Pacific, and a more El Niño–like mean state of the tropical Pacific with a weaker west–east temperature contrast. Meanwhile, the SST variance decreases in the central and eastern tropical Pacific, and ENSO becomes less energetic. They further examined their hypothesis for the change in ENSO variability by performing simulations using an intermediate-complexity coupled model. Overall, their results demonstrated that changes in the mean state of the coupled system can contribute to change ENSO variance.

The building evidence, therefore, calls for more comprehensive investigation of the influence of land surface processes on the mean, seasonal cycle, and interannual variability of the coupled ocean–atmosphere system. It seems imperative, therefore, to address the impact of land surface processes on climate within a fully coupled ocean–atmosphere framework. The present paper narrows down on an important aspect of this complex problem: the impact of biogeophysical (vegetation and soil moisture) processes on the sensitivity of global climate mean state and its variability on interannual time scales with a particular focus on the ocean–atmosphere–land feedback processes. We conduct numerical experiments using a CGCM in which the atmospheric component offers a choice of different land surface schemes. The scientific questions addressed in this study are the extent to which 1) interactive soil moisture and vegetation biophysical processes affect the global-mean climate and climate variability when ocean–atmosphere coupling is considered and 2) ocean–atmosphere interactions modify the strength of local land–atmosphere interactions (the indirect effect of land surface processes).

The main body of the text is organized into five sections. Section 2 provides a brief introduction to the observational datasets, numerical models used, and land surface schemes choices in the atmospheric model. Section 3 demonstrates the sensitivity of global-mean climate and climate variability to different land surface schemes by comparing simulated results. Section 4 presents a summary, discussion, and the conclusions.

2. Datasets, model, and methodology

a. Observational datasets

We use monthly-mean global precipitation fields from the Climate Prediction Center (CPC) Merged Analysis of Precipitation (CMAP; Xie and Arkin 1997). CMAP, which merges observations from rain gauges and estimates from several satellite-based algorithms (infrared and microwave), covers the period 1979–2009. We also use monthly-mean global SST fields from National Oceanic and Atmospheric Administration (NOAA) Extended Reconstructed SST (ERSST) V3b (Smith et al. 2008). This dataset was compiled based on the International Comprehensive Ocean–Atmosphere Data Set (ICOADS) SST data and on the application of improved statistical methods that allow for stable reconstruction using sparse data. The period used in this study covers from 1901 to 2000. Both the CMAP and NOAA SST datasets are available online (http://www.esrl.noaa.gov/psd/), and we interpolated the fields in both datasets into a 2.5° longitude by 2.0° latitude grid to match the horizontal resolution of the AGCM.

b. Atmospheric model: UCLA AGCM

The UCLA AGCM has been used in many climate studies (e.g., Xiao and Mechoso 2009a,b; Ma et al. 2010, 2011). The model's parameterization of cumulus convection, including its interaction with the planetary boundary layer (PBL), follows the prognostic version of Arakawa and Schubert (1974) (Pan and Randall 1998). The parameterization of radiative processes is based on Harshvardhan et al. (1987, 1989), and the parameterization of PBL processes is based on the mixed-layer approach of Suarez et al. (1983), as revised by Li et al. (2002). Surface heat fluxes are calculated following the bulk formula proposed by Deardorff (1972) and modified by Suarez et al. (1983). The model also includes the parameterizations of prognostic cloud liquid water and ice (Köhler 1999; Ma et al. 2012) and the effects of cumulus clouds on the radiation calculations. A more detailed description of the model can be found in Arakawa (2000), Mechoso et al. (2000), or online (at http://www.atmos.ucla.edu/~mechoso/esm/agcm.html). In the present study, we use AGCM version 7.1 with a horizontal resolution of 2.5° latitude and 2° longitude and 29 layers in the vertical. The distributions of greenhouse gases, sea ice, and ocean surface albedo are all prescribed corresponding to a monthly observed climatology. The cyclically monthly varying SST fields for the AGCM

experiments are from the climatology compiled by Reynolds and Smith (1995).

c. Oceanic model: MIT GCM

The oceanic component of the CGCM is the Massachusetts Institute of Technology (MIT) GCM (Marshall et al. 1997; http://mitgcm.org). In the model configuration, the grid has 360×224 horizontal grid cells. Zonal grid spacing is 1° of longitude, and meridional grid spacing is 0.3° of latitude within $\pm 10°$ of the equator, increasing to 1° latitude poleward of 30°. There are 46 levels in the vertical with thicknesses ranging from 10 m near the surface to 400 m near the maximum depth of 5815 m. Ocean regions north of 73°N and south of 73°S are not represented in order to permit a 1-h integration time step. The model employs the K-profile parameterization (KPP) vertical mixing scheme of Large et al. (1994) and the isopycnal mixing schemes of Redi (1982) and Gent and McWilliams (1990) with surface tapering as per Large et al. (1997). Laplacian diffusion and friction are used except for horizontal friction, which is biharmonic. Lateral boundary conditions are closed. No-slip bottom, free-slip lateral, and free surface boundary conditions are employed. Surface freshwater fluxes are applied as virtual salt fluxes.

d. Land surface component in the UCLA AGCM

The UCLA AGCM currently offers two choices for land surface component: one specifies most surface conditions–processes and another presents interactive land–atmosphere interactions. The key differences between the two schemes presenting the land–atmosphere interactions include 1) the representation of surface albedo and 2) the way the surface momentum, heat, and water fluxes are calculated. The first one is a simple land scheme (SLS). In SLS, the surface albedo is cyclically varying monthly climatology obtained from satellite remote sensing. For surface momentum and heat fluxes in SLS, the calculation of bulk aerodynamic formulas of latent and sensible heat fluxes are based on Suarez et al. (1983). The formulations are the same over land and over ocean. The efficiency factor β, which represents the ratio of actual and potential evaporations, is prescribed based on observational data, and the spatial adjustments were conducted according to results in long-term integrations (i.e., "tuning," no interactive soil moisture or soil layers). This implies no memory (e.g., deep soil moisture or temperature anomalies) from the land component. Ground temperature (skin temperature) over land is predicted from an energy balance of net surface shortwave radiation, net surface longwave radiation, sensible heat, and latent heat fluxes (no ground heat flux).

As an alternative to the simple land scheme, the AGCM incorporates the first generation of the Simplified Simple Biosphere Model (SSiB; Xue et al. 1991). This SSiB version has three soil layers and one vegetation layer. Soil moisture of the three soil layers, interception water store for the canopy, deep soil temperature, ground temperature, and canopy temperature are all predicted based on the water and energy balance at canopy and soil. Three aerodynamic resistances control the heat and water fluxes between the canopy layer air space and 1) canopy leaves, 2) soil surface, and 3) the reference PBL height. The resistance values are determined in terms of vegetation properties, ground conditions, and bulk Richardson number according to the Monin–Obukhov similarity theory (Paulson 1970; Businger et al. 1971; Deardorff 1972; Sellers et al. 1986; Xue et al. 1991, 1996a). The surface albedo is calculated through a two-stream radiative transfer scheme and has diurnal variations representing the change of net solar radiation in the canopy layer due to vegetation properties. Several data sources (Dorman and Sellers 1989; Xue et al. 1996b) have been used to determine the vegetation types that specify monthly climatological land surface properties (e.g., leaf area index, green leaf fraction, and surface roughness length). Over ocean, calculations of surface momentum, heat, and water fluxes are the same in SLS and in SSiB.

Details of coupling processes between UCLA AGCM and MIT OGCM or between UCLA AGCM and SSiB–SLS are given in Cazes-Boezio et al. (2008), Xue et al. (2010), and Ma et al. (2010), respectively. The atmospheric initial conditions for AGCM and CGCM experiments were taken from a previous, multiyear model run starting from 1 October 1982. The oceanic initial conditions for MIT GCM were taken from multiyear model run of the experiments conducted in Cazes-Boezio et al. (2008).

e. Experiments

We performed four CGCM and AGCM experiments with selection of SLS and SSiB. The CGCM experiments are 120 years long and will be referred to as CGCM/SLS and CGCM/SSiB. Although the oceanic GCM initial condition is taken from a previous multiyear run, results for the first 20 years are not included in the analysis. The AGCM experiments are 30 years long and will be referred to as AGCM/SLS and AGCM/SSiB.

3. Sensitivity of climate mean state and interannual variability in the tropics

a. Annual-mean climatology

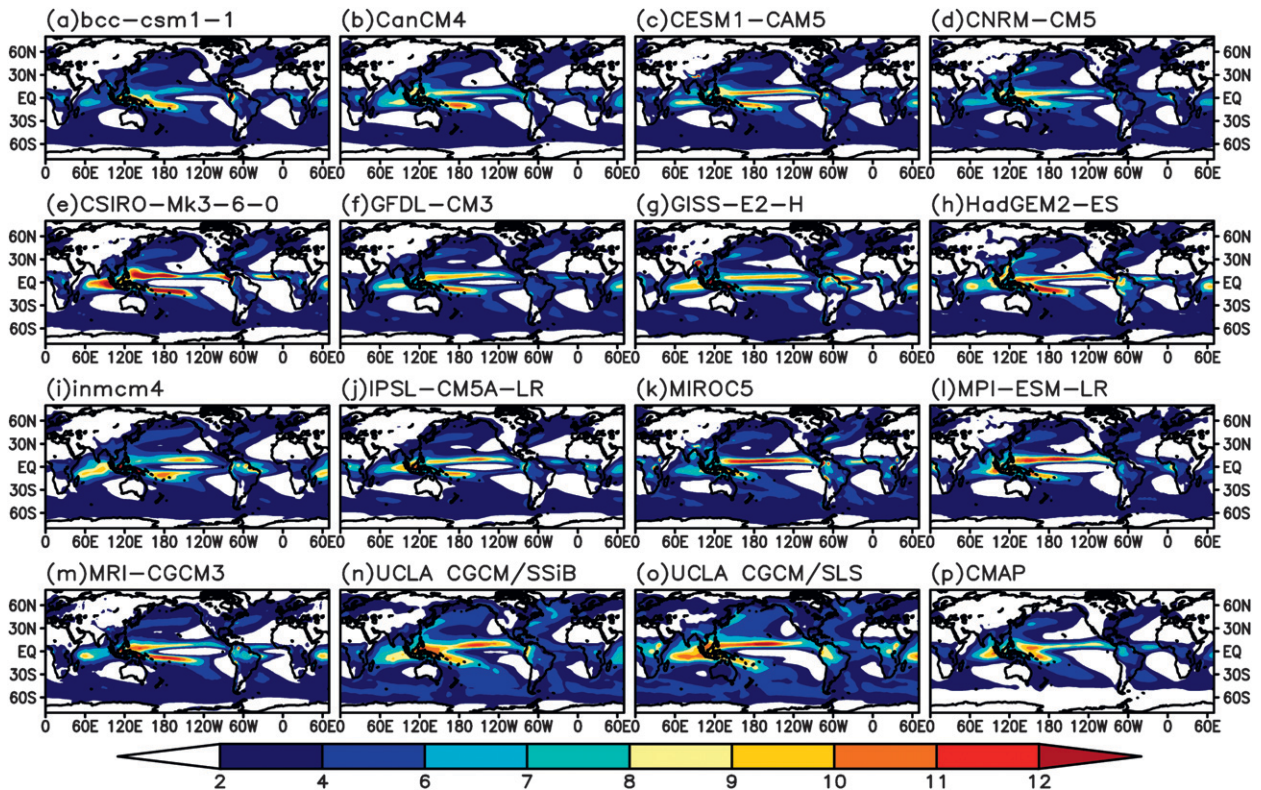We start by giving a primary assessment of how the performance of our CGCM compares to other

FIG. 1. Annual-mean precipitation (mm day^{-1}) (p) from CMAP and model simulations of UCLA (n) CGCM/SSiB and (o) CGCM/SLS, as well as (remaining panels) historical experiments from WCRP CMIP5 multimodel datasets. See Table 1 for the list of models.

contemporary models. Figures 1a–m show the annual-mean precipitation by some of the 13 models participating in the "historical" experiment (twentieth-century run) of the World Climate Research Programme (WCRP) phase five of the Coupled Model Intercomparison Project (CMIP5; see Table 1 for a list of models), whereas Figs. 1n–p display the annual-mean precipitation from CGCM/SLS, CGCM/SSiB, and the observational estimates from CMAP, respectively. In reference to the CMAP field, both CGCM/SLS and CGCM/SSiB and all the selected WCRP CMIP5 CGCMs reproduce, with different degrees of success, the main features of global precipitation: intertropical convergence zone (ITCZ), South Pacific convergence zone (SPCZ), South Atlantic convergence zone (SACZ), major continental monsoons, and midlatitude storm tracks. There are, however, significant errors as well as intermodel differences. All simulations overestimate global-mean precipitation and show a secondary, unrealistic ITCZ south of the equatorial Pacific, which is the well-known double-ITCZ syndrome (e.g., Mechoso et al. 1995; Lin 2007). Several models also show stronger precipitation over the central Pacific Ocean and weaker Atlantic ITCZ over South America and the western Atlantic. The performance of

both CGCM/SLS and CGCM/SSiB is clearly comparable with that of other state-of-the-art CGCMs. CGCM/SSiB, in particular, produces one of the most realistic distributions of precipitation over the western Pacific, especially in the warm pool and SPCZ regions, and it also obtains a weaker double ITCZ. In view of the encouraging performance of our CGCM, we concentrate next on the sensitivity of its simulated global climate to the choice of parameterizations of land surface processes. In the remainder of the paper, we refer to the differences (CGCM/SSiB − CGCM/SLS) and (AGCM/SSiB − AGCM/SLS) as the CGCM and AGCM sensitivities, respectively.

Figure 2 presents the CGCM and AGCM sensitivities to land surface processes of annual-mean net fluxes of shortwave radiation, longwave radiation, sensible heat flux, and latent heat flux at the surface. The values in the areas with color are statistically significant at the 95% confidence level according to a two-tailed t test (100 members for the CGCM and 30 members for the AGCM runs) based on the formulation presented in Wilks (2006). In our sign convention for model output, positive values of net shortwave flux at the surface represent a net energy sink for the atmosphere (gain for the ocean), while those

TABLE 1. List of selected models, model resolutions, and their originating groups of the historical experiment (twentieth-century runs) from the WCRP CMIP5 archives (for more detailed description of the models, see http://cmip-pcmdi.llnl.gov/cmip5/index.html.

CMIP5 model acronym	CMIP5 model name	Modeling group(s)	AGCM resolutions (lon × lat, level)
BCC CSM1-1	Beijing Climate Center (BCC) CSM1-1	Beijing Climate Center, China Meteorological Administration	128 × 64, L26
CGCM4	Canadian Centre for Climate Modeling and Analysis (CCCma) Coupled General Circulation Model version 4	Canadian Centre for Climate Modeling and Analysis	128 × 64, L35
CESM1-CAM5	Community Earth System Model version 1 Community Atmosphere Model version 5	National Center for Atmospheric Research	288 × 192, L30
CNRM-CM5	Centre National de Recherches Météorologiques Coupled Global Climate Model version 5	Centre National de Recherches Meteorologiques/Centre Europeen de Recherche et Formation Avancées en Calcul Scientifique	256 × 128, L31
CSIRO Mk3–6-0	Commonwealth Scientific and Industrial Research Organisation Mark version 3–6-0	Commonwealth Scientific and Industrial Research Organization in collaboration with the Queensland Climate Change Centre of Excellence	192 × 96, L18
GFDL CM3	Geophysical Fluid Dynamics Laboratory Climate Model version 3	Geophysical Fluid Dynamics Laboratory	144 × 90, L48
GISS-E2-H	Goddard Institute for Space Studies Model E2-H	National Aeronautics and Space Administration (NASA) Goddard Institute for Space Studies	144 × 90, L29
HadGEM2-ES	Hadley Centre Global Environmental Model version 2-ES	Met Office Hadley Centre	192 × 145, L38
INM-CM4	Institute of Numerical Mathematics Coupled Model version 4	Institute for Numerical Mathematics	180 × 120, L21
IPSL CM5A-LR	L'Institut Pierre-Simon Laplace Coupled Model version 5A (low resolution)	L'Institut Pierre Simon Laplace	96 × 96, L39
MIROC5	Model for Interdisciplinary Research on Climate 5	Atmosphere and Ocean Research Institute (University of Tokyo), National Institute for Environmental Studies, and Japan Agency for Marine-Earth Science and Technology	256 × 128, L40
MPI-ESM-LR	Max Planck Institute Earth System Model (low resolution)	Max Planck Institute	192 × 96, L47
MRI CGCM3	Meteorological Research Institute Coupled General Circulation Model version 3	Meteorological Research Institute	320 × 160, L35

of net surface longwave, sensible, and latent heat fluxes represent a net energy source for the atmosphere (sink for the ocean). Tables 2 and 3 present global statistics for the sensitivities in energy, water fluxes, and total cloud cover. According to Fig. 2, the spatial patterns of the CGCM and AGCM sensitivities tend to be similar over land but different over the oceans, especially in the Pacific (Table 4). The sensitivity of net surface shortwave radiation (Fig. 2a) in the CGCM has larger magnitudes over the Pacific than in the AGCM, with opposite signs between the western and southeastern tropical regions. The very large values in the CGCM over the southeastern Pacific are due to a reduction of stratocumulus in the simulation with SSiB far away from the coast, where the simulation with SLS show the stratocumulus cover extending too far west. Such features are consistent with warmer underlying SST and weaker large-scale subsidence above cloud top

in CGCM/SSiB (as is shown in Figs. 3, 6). The sensitivities of longwave radiation flux at the surface are positive over the continents with both models, indicating higher land skin temperatures in the simulations with SSiB than in those with SLS. The increase in longwave radiation flux over land with SSiB is ~65%. Over the oceans, the CGCM and AGCM sensitivities are weaker than over land, with patterns that are similar except over the Indian Ocean, where signs are opposite. The sensitivities of sensible heat flux at the surface indicate that values of this field in both CGCM/SSiB and AGCM/SSiB tend to be generally higher over tropical land regions than in CGCM/SLS and AGCM/SLS, respectively, and lower in most desert and high-latitude lands. Although the sensitivities in sensible heat flux at the surface tend to be numerally smaller than those of other surface fluxes, the percentage of absolute change in the individual fields is
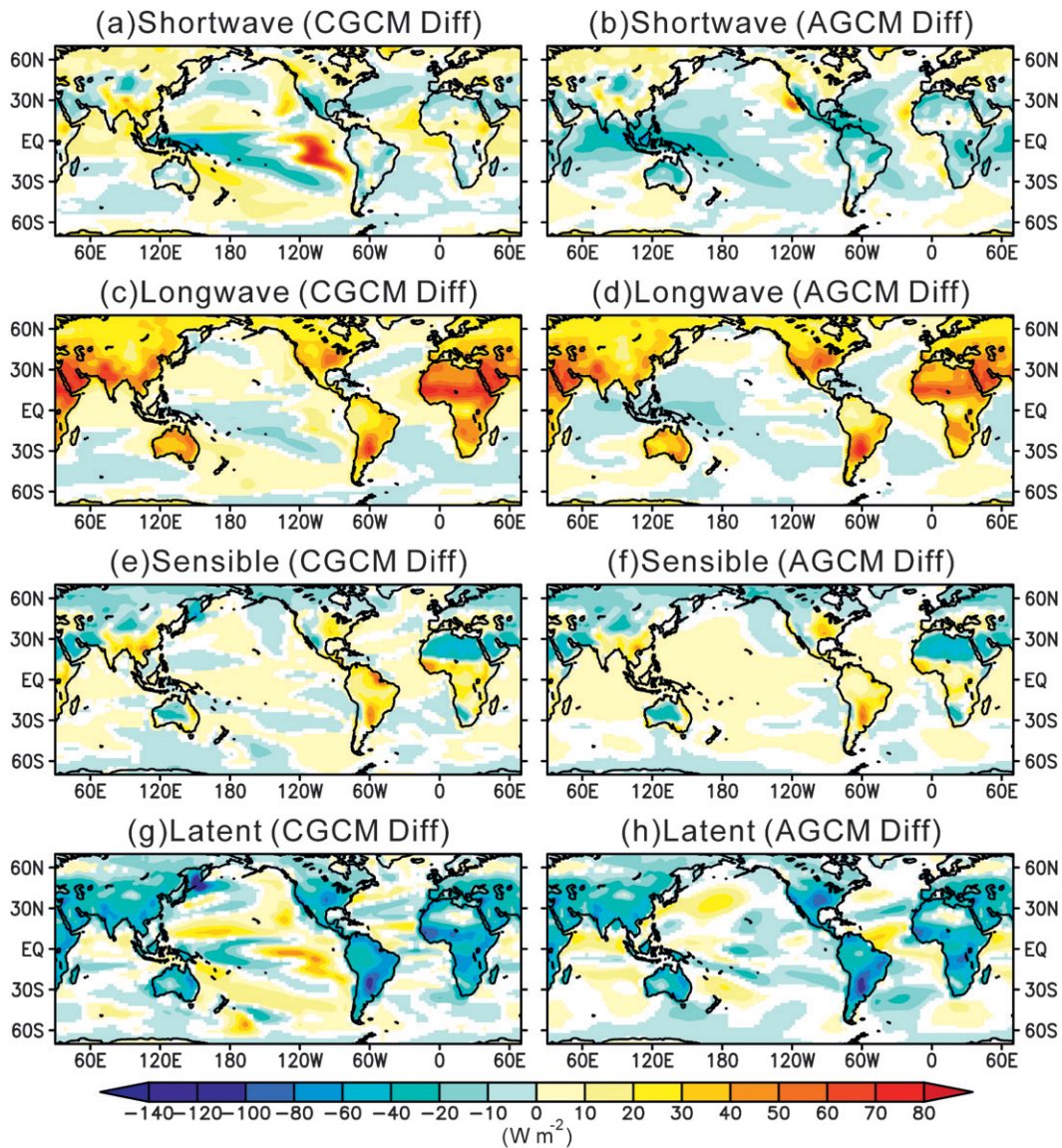
FIG. 2. Differences of annual-mean (a) net shortwave flux at surface (W m^{-2}), (c) net longwave flux at surface (W m^{-2}), (e) surface sensible heat flux (W m^{-2}), and (g) surface latent heat flux (W m^{-2}) between CGCM/SSiB and CGCM/SLS (CGCM sensitivity; SSiB − SLS). Also shown here are the differences of annual-mean (b) net shortwave flux at surface (W m^{-2}), (d) net longwave flux at surface (W m^{-2}), (f) surface sensible heat flux (W m^{-2}), and (h) surface latent heat flux (W m^{-2}) between AGCM/SSiB and AGCM/SLS (AGCM sensitivity; SSiB − SLS). Values where differences are statistically significant at the 95% confidence level are color shaded.

very significant according to Tables 2 and 3. Over the oceans, the sensitivity of longwave radiation and sensible heat flux in both the CGCM and AGCM are rather featureless. The sensitivity of latent heat flux at the surface is generally negative over land in both models, indicating weaker evaporation in the simulations with SSiB than in those with SLS. The reduction in evaporation over land with SSiB is ~45%.

Figure 3 presents the CGCM and AGCM sensitivities to land surface processes of annual-mean precipitation, cloud cover, and SST (the latter for the CGCM only). In both CGCM/SSiB and AGCM/SSiB, precipitation is reduced by ~34% over land in reference to CGCM/SLS and AGCM/SLS, respectively (Tables 2, 3). Over the oceans, the most outstanding feature is in the CGCM results, which shows precipitation, cloud cover, and SST significantly higher with SSiB over the central and western equatorial Pacific along the ITCZ and the SPCZ (Table 4). Also, precipitation and clouds with SSiB is significantly decreased in the southern and northern

TABLE 2. Percentage of absolute change in the annual-mean total precipitation, cumulus precipitation, stratiform precipitation, total cloud cover, net surface shortwave flux, net surface longwave flux, surface sensible heat, and surface latent heat between the CGCM/SSiB and CGCM/SLS experiments averaged over the globe, global ocean, and global land. The percentage of absolute change is defined as $100\% \times |\text{VAR}_{\text{CGCM/SSiB}} - \text{VAR}_{\text{CGCM/SLS}}|/|\text{VAR}_{\text{CGCM/SLS}}|$, where VAR is the individual variable listed in the left column.

% of change variables	Global mean	Global land mean	Global ocean mean
Total precipitation	23.97	34.17	20.79
Cumulus precipitation	42.16	63.33	35.40
Stratiform precipitation	20.49	27.87	18.19
Total cloud cover	8.96	10.62	8.55
Net surface shortwave flux	6.24	9.12	5.33
Net surface longwave flux	28.01	76.86	8.81
Surface sensible heat flux	82.82	95.03	53.55
Surface latent heat flux	15.24	45.93	7.51

TABLE 3. As in Table 2, but between the AGCM/SSiB and AGCM/SLS experiments The percentage of absolute change is defined as $100\% \times |\text{VAR}_{\text{AGCM/SSiB}} - \text{VAR}_{\text{AGCM/SLS}}|/|\text{VAR}_{\text{AGCM/SLS}}|$.

% of change variables	Global mean	Global land mean	Global ocean mean
Total precipitation	18.57	34.65	12.36
Cumulus precipitation	40.90	74.36	25.58
Stratiform precipitation	25.29	39.73	20.63
Total cloud cover	6.93	8.96	6.25
Net surface shortwave flux	5.16	9.86	3.67
Net surface longwave flux	21.47	64.78	5.38
Surface sensible heat flux	74.98	86.09	46.85
Surface latent heat flux	15.20	45.85	6.76

parts of the ocean, which is associated with colder SSTs. This feature indicates the strong association among SST, convection, and clouds. The sensitivity in precipitation is also clearly associated with that in shortwave radiation (Fig. 2a), as less clouds allow more solar radiation to penetrate, which affects the net radiation at surface and leads to increased latent heat flux (Fig. 2g).

The sensitivity of SST in the CGCM over the Pacific also shows a clear large-scale pattern where two feature stand out with SSiB. First, the entire tropical region is warmer, with higher values in the eastern part of the basin; this is consistent with a decrease in the longitudinal SST gradient. Second, the northwest Pacific becomes significant colder. Taken together, these features are consistent with a decrease in the intensity of the North Pacific high and gyre (shown in Fig. 6), which affects the advection of ocean temperature and coastal upwelling. The Atlantic Ocean also shows those two features albeit with modest amplitudes; the Indian Ocean becomes slightly warmer. The different sensitivity between the CGCM and AGCM simulations suggests that ocean–atmosphere coupling can significantly affect the impact of different land surface processes on precipitation, cloud cover, and other fields (Table 4), which also have

substantial impact on the SST. On the other hand, feedback processes over the equatorial ocean regions in the AGCM are hampered because SSTs are prescribed.

It is well known that changes in the surface heat fluxes over land resulting from the use of different land surface schemes can significantly affect the intensity of deep convection (e.g., Betts et al. 1996; Xue et al. 2010; Ma et al. 2010). Deep convection over tropical and subtropical lands is less intense in the simulation with SSiB (Tables 2, 3) mainly because of a more stable atmosphere. Smaller values of convective available potential energy (CAPE) result from the higher surface sensible and lower latent heat fluxes at the surface (larger Bowen ratios), which result in a deeper and dryer PBL (not shown here). Figure 4 shows the annual- and zonal-mean profiles of diabatic heating over land (heating at the lowest model level corresponding to the PBL is not shown in Fig. 4). The heating associated with cumulus convection ($\dot{Q}_{\text{Cum}}$), large-scale condensation ($\dot{Q}_{\text{LS}}$), and radiative heating ($\dot{Q}_{\text{Rad}}$; both shortwave and longwave), all contribute to total diabatic heating (K day^{-1}) above PBL,

$$\dot{Q}_T = \dot{Q}_{\text{Cum}} + \dot{Q}_{\text{LS}} + \dot{Q}_{\text{Rad}}. \tag{1}$$

The vertical structures of $\dot{Q}_T$ in CGCM/SSiB and CGCM/SLS have similar patterns, but the values have different magnitudes. The simulation with SSiB shows

TABLE 4. As in Tables 2 and 3, but for the tropical Pacific Ocean (30°S–30°N, 120°E–70°W).

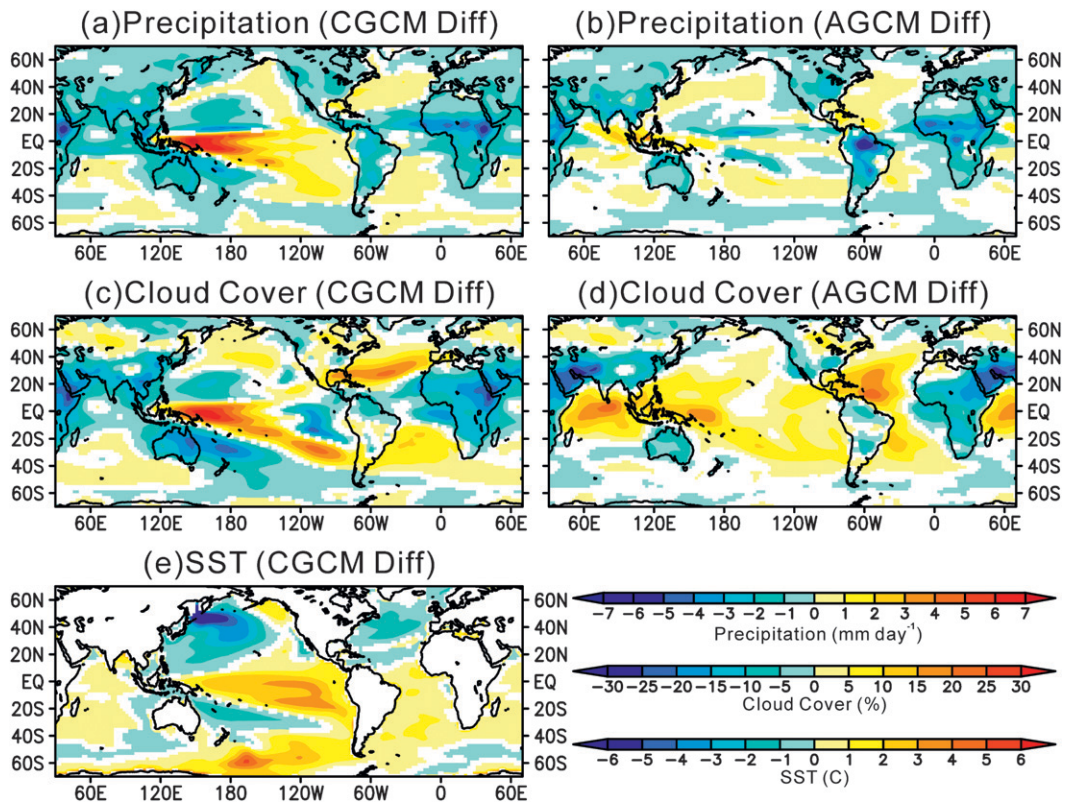| % of change variables	$100\% \times \dfrac{|\text{VAR}_{\text{CGCM/SSiB}} - \text{VAR}_{\text{CGCM/SLS}}|}{|\text{VAR}_{\text{CGCM/SLS}}|}$	$100\% \times \dfrac{|\text{VAR}_{\text{AGCM/SSiB}} - \text{VAR}_{\text{AGCM/SLS}}|}{|\text{VAR}_{\text{AGCM/SLS}}|}$
Total precipitation	33.53	13.06
Cumulus precipitation	48.21	26.39
Stratiform precipitation	26.06	42.64
Total cloud cover	13.93	8.37
Net surface shortwave flux	8.29	3.98
Net surface longwave flux	12.25	6.21
Surface latent heat flux	8.56	5.48

FIG. 3. Differences of annual-mean (a) precipitation (mm day^{-1}), (c) cloud cover (%), and (e) sea surface temperature (°C) between CGCM/SSiB and CGCM/SLS (CGCM sensitivity; SSiB − SLS). Also shown here are the differences of annual-mean (b) precipitation (mm day^{-1}) and (d) cloud cover (%), between AGCM/SSiB and AGCM/SLS (AGCM sensitivity; SSiB − SLS). Values where differences are statistically significant at the 95% confidence level are color shaded.

weaker heating (cooling) in the tropics (polar regions) by about ~0.3 K day^{-1}. In the tropical and subtropical continents, the heating profiles associated with both cumulus convection and large-scale condensation show significant sensitivities. The cumulus convection is much weaker in CGCM/SSiB, which suggests less CAPE, while the large-scale condensation is stronger in the tropics and weaker in the subtropics, which tends to be opposite to that of cumulus convection. In the tropics, the large-scale heating shows an intense center in the lower troposphere (700 hPa). Radiative cooling in CGCM/SSiB is less intense in the lower troposphere in the tropics and subtropics, as well as in the midtroposphere over the polar regions. This characteristic of land–atmosphere interactions has also been found in Xue (1997), indicating the dominant process in the land–atmosphere interactions is the hydrological cycle, although the radiative process may trigger the feedback process.

In view of the significant sensitivity in the atmospheric heating, it is not surprising to find strong sensitivities in the general circulation (e.g., Gill 1980; Rodwell and Hoskins 2001). For both the CGCM and AGCM

simulations, Fig. 5 displays the annual-mean divergent winds and velocity potential in the upper troposphere (150 hPa). According to Fig. 5, there is a center of large-scale divergence–rising motion over the western Pacific–Maritime Continent in all cases. The center is weaker in the AGCM and too far west compared to the observation in CGCM/SLS (Fig. 5d), in which the equatorial cold tongue is too strong and extends too far west (Fig. 1o). The regions of upper-level convergence–sinking motion with SSiB and with SLS show an interesting difference. The two simulations with SSiB (Figs. 5a,c) depict a major center of convergence over the Namibian coast and Africa continent (Sahara Desert). The simulations with SLS, by contrast, depict different patterns. AGCM/SLS (Fig. 5b) has centers of convergence along the eastern Pacific and subtropical Atlantic, while CGCM/SLS shows (Fig. 5d) convergence over the entire tropical and subtropical South America. The simulations with SSiB are also closer to observations (not shown here).

Figure 6 presents the annual-mean velocity and streamfunction in the lower troposphere (850 hPa). In the AGCM simulations (Figs. 6a,b), the low-level
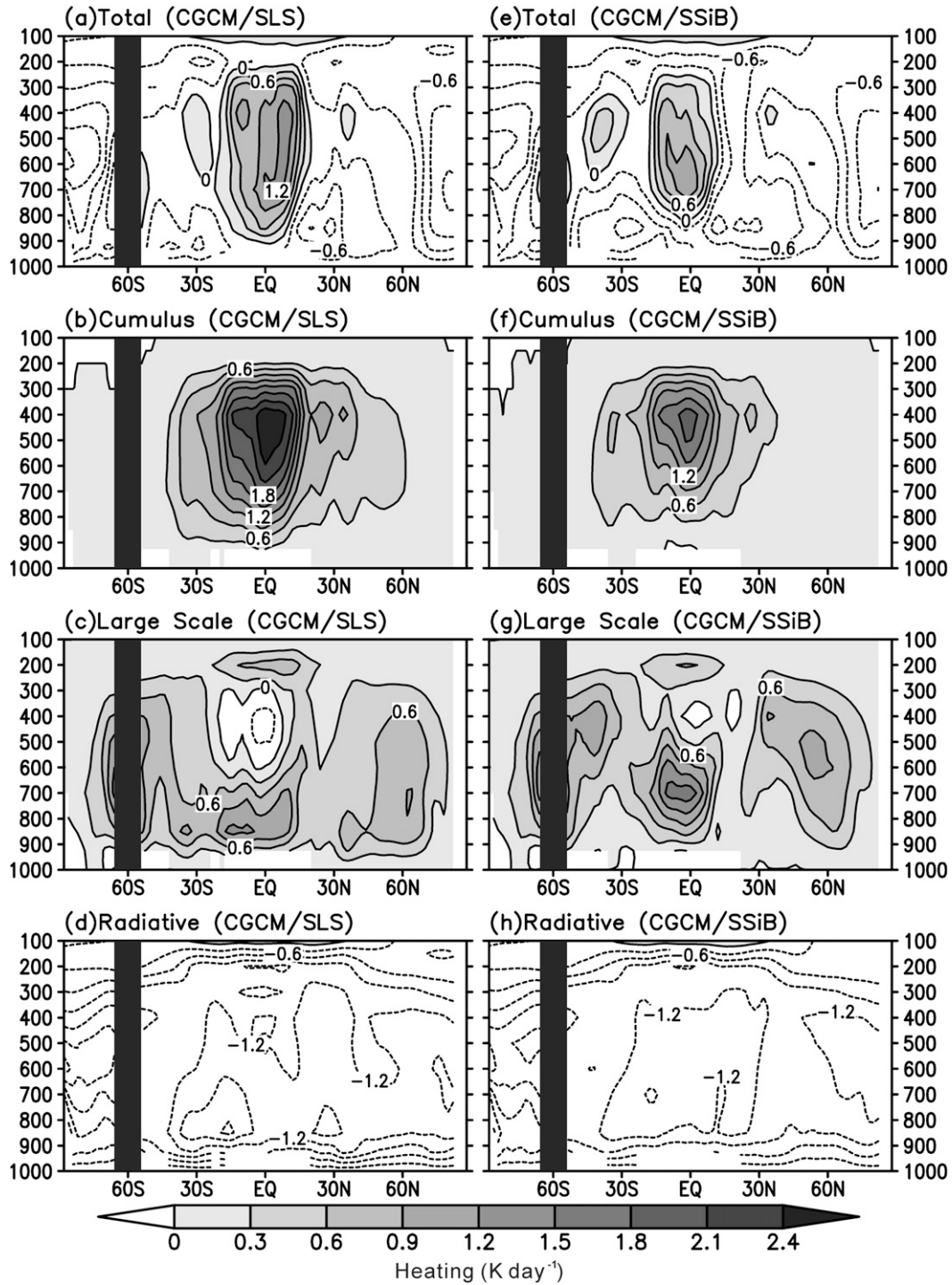
FIG. 4. Zonal mean of the annual-mean (a),(e) total diabatic heating; (b),(f) cumulus heating; (c),(g) large-scale heating; and (d),(h) radiative heating from (left) CGCM/SLS and (right) CGCM/SSiB. The contour interval is 0.3 K day^{-1}.

circulations are very similar over the oceans, as is expected since the underlying SST is identical. The CGCM simulations (Figs. 6c,d) produce different SSTs distributions. The equatorial easterly trades are weaker over

the western Pacific in CGCM/SSiB by ~20%, and the equatorial SST is also warmer (Fig. 3e) partly because of the weaker equatorial upwelling (weaker trades and surface wind stress). There are also significant changes
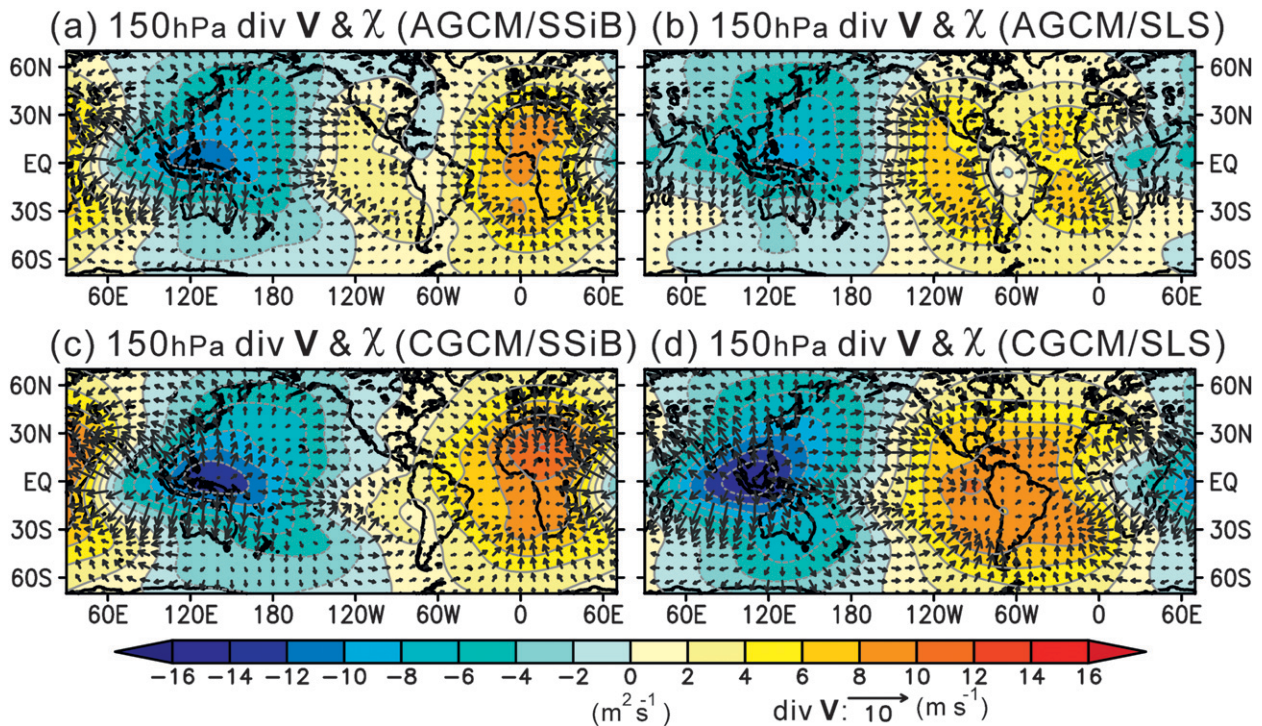
FIG. 5. Annual mean of divergent winds (m s^{-1}; arrows) and velocity potential (m^2 s^{-1}; color shades and contours) at 150 hPa from (a) AGCM/SSiB, (b) AGCM/SLS, (c) CGCM/SSiB, and (d) CGCM/SLS.

in the subtropical highs, which are less zonal in CGCM/SSiB than in CGCM/SLS, especially in the Pacific. Taking together the changes in the upper (Fig. 5) and lower (Fig. 6) troposphere, simulations with SSiB show weaker Hadley (weaker subtropical highs) and Walker circulations (weaker trade winds). Also, the weaker south Pacific high (less subsidence) and warmer SST are consistent with the reduced stratocumulus over the southeast Pacific (Fig. 3c).

The surface wind stress is also strongly sensitive to the representation of land surface processes (Fig. 7) as it is closely linked to the low-level circulation. This sensitivity is larger in the CGCM experiments as the SSTs also changed, especially over the Pacific. Over the equatorial part of this ocean, easterly and southeasterly trades are weaker in CGCM/SSiB than in CGCM/SLS. The weaker trades in CGCM/SSiB result in a reduction of the excessive westward extension of the equatorial cold tongue in CGCM/SLS (Figs. 3e), and therefore the double-ITCZ bias is alleviated with SSiB (Fig. 3c).

Since surface wind stress is sensitive to the representation of land surface processes, the upper-ocean wind-driven currents must be sensitive too. Figure 8 displays north–south vertical cross sections of the zonal-mean speed in the upper ocean from CGCM/SSiB and their sensitivity for the three tropical basins. In the tropical

Pacific, the mean field in CGCM/SSiB clearly shows the surface equatorial current, equatorial undercurrent, and north equatorial countercurrent. The sensitivity pattern in this ocean is rather complex, including a weakening of the undercurrent speed at deeper levels and a strengthening at upper levels. This feature reflects a shallower and weaker undercurrent (shown in Fig. 10). The north equatorial counter current also weakens with SSiB. In the Atlantic basin, the sensitivity consists of an intensification of the mean pattern. In the Indian basin, the sensitivity is very weak.

The results in Fig. 8 suggest that, at least in the Pacific, the CGCM/SSiB produces a more realistic simulation of the upper ocean. This impression is confirmed in Fig. 9, which presents the deviation of the annual-mean SST from the zonal mean along the equator in both Pacific and Atlantic basins from both observations and simulations. The zonal SST gradient shown in Fig. 9 is closely associated with the surface wind speed intensity along the equator (e.g., Lindzen and Nigam 1987). Together with the deep convection in the western Pacific, this zonal SST gradient drives the equatorial easterlies, which are integral part of the Walker circulation (Gill 1980). In the observation, the SST shows a strong zonal gradient between 160°E and 120°W in the Pacific basin and between 45° and 5°W in the Atlantic basin, with warm pools in the
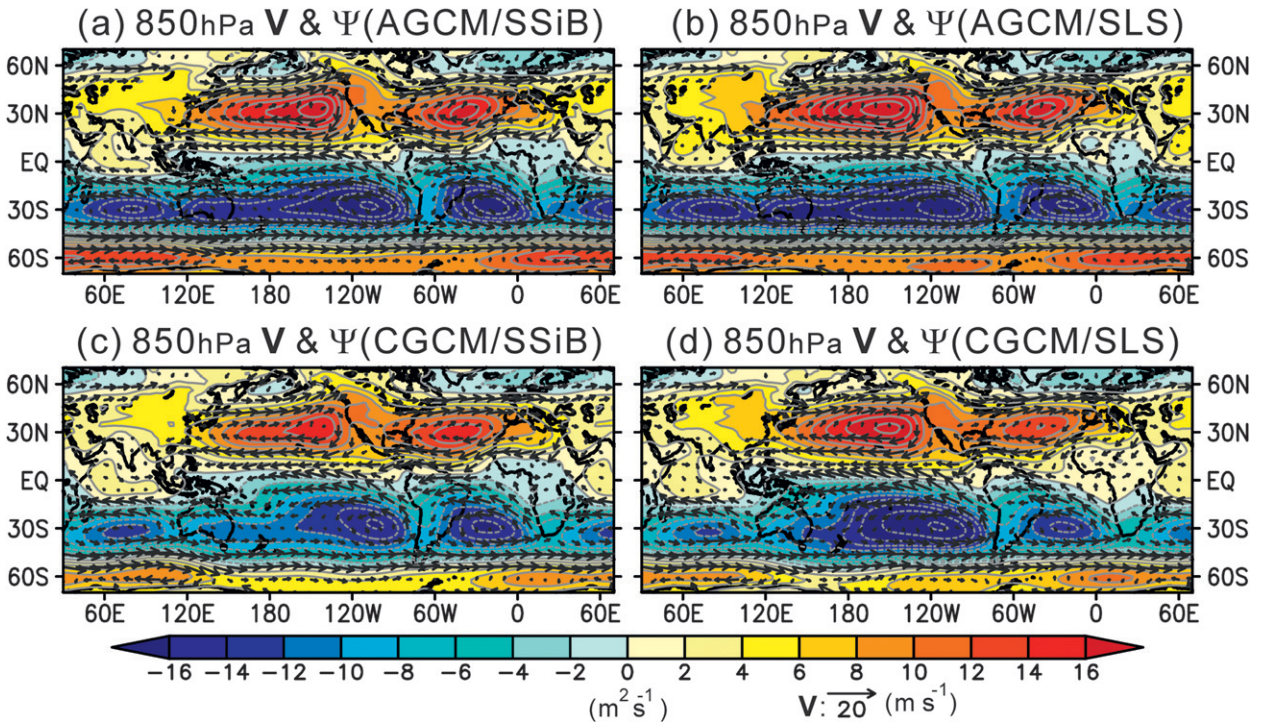
FIG. 6. As in Fig. 5, but for velocity and streamfunction at 850 hPa.

west and equatorial cold tongues in the east. Starting in the equatorial Pacific, both CGCM simulations show zonal SST gradients that are similar to the observation in the central part of the basin. CGCM/SLS produces an unrealistically strong SST gradient over the western Pacific warm pool, which is consistent with the stronger equatorial easterly trades and over extended cold tongue. In the eastern Pacific, the simulated SSTs are too warm,
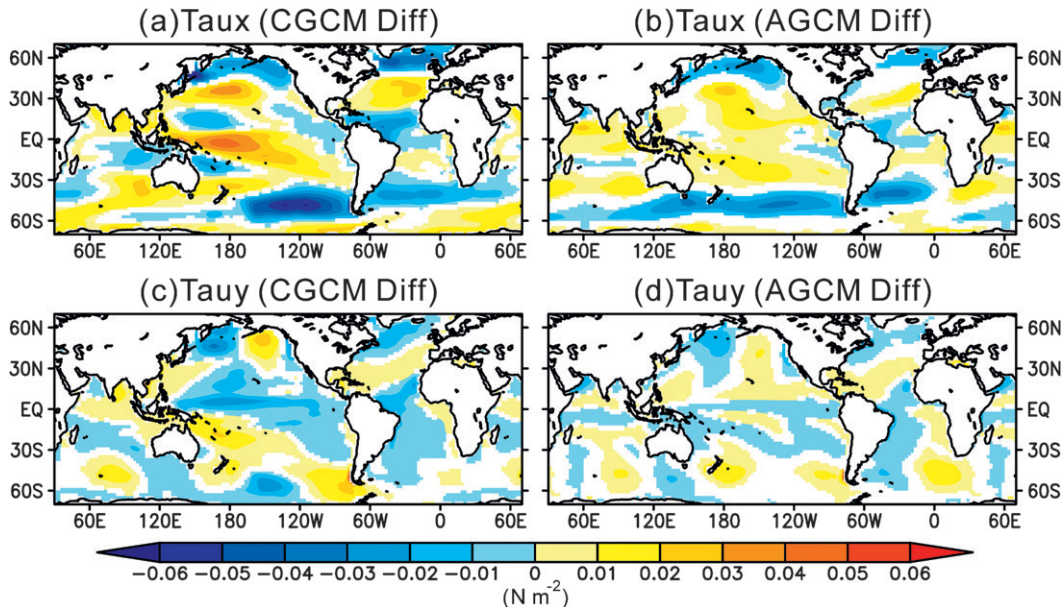

FIG. 7. Differences of annual-mean (a) surface zonal wind stress (N m^{-1}) and (c) surface meridional wind stress (N m^{-1}) between CGCM/SSiB and CGCM/SLS (CGCM sensitivity; SSiB − SLS). (b),(d) As in (a),(c), but between AGCM/SSiB and AGCM/SLS (AGCM sensitivity; SSiB − SLS). Values where differences are statistically significant at the 95% confidence level are color shaded.
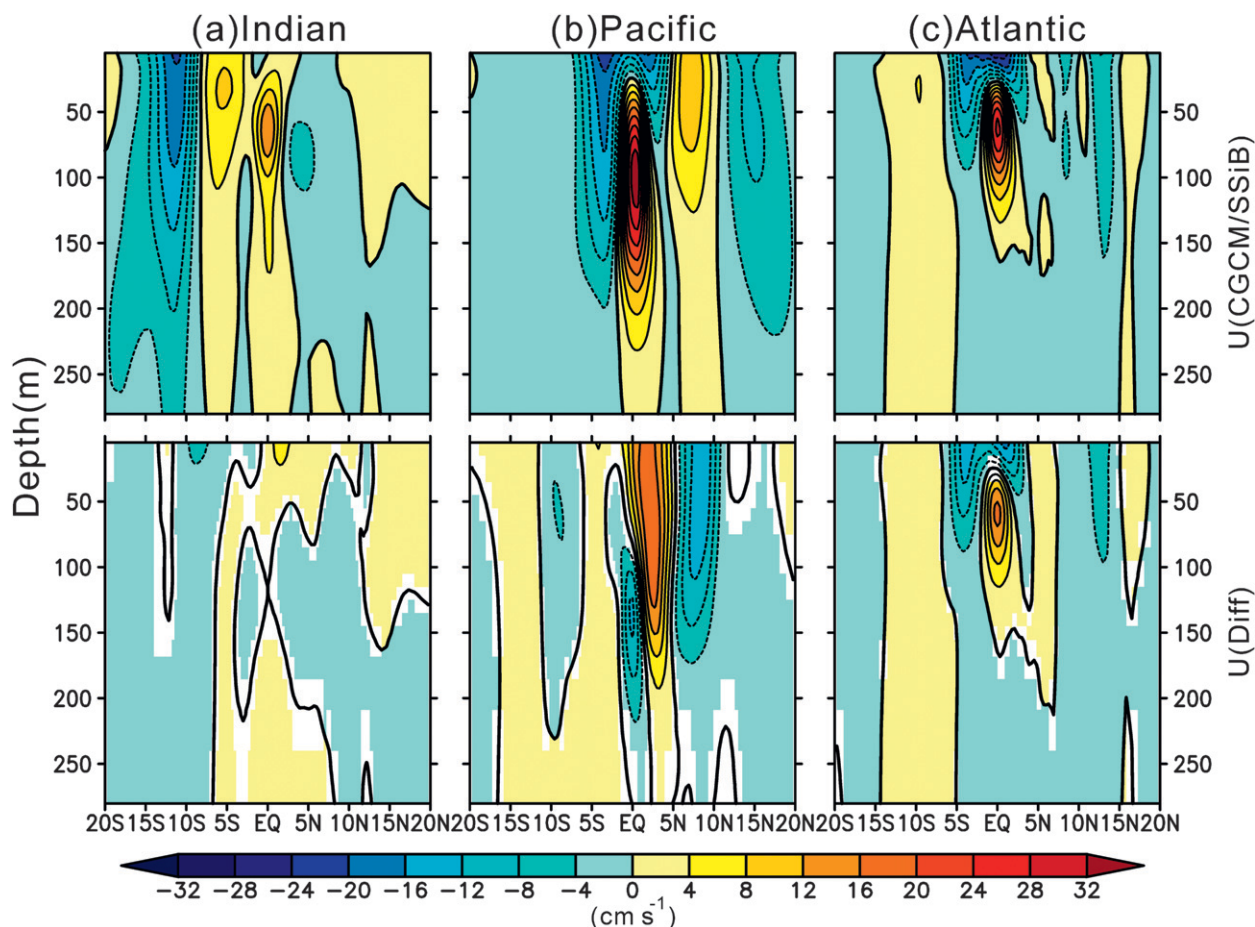
FIG. 8. (top) Annual-mean profiles of oceanic zonal-mean current speed (cm s^{-1}) averaged over (a) Indian basin (40°–110°E), (b) Pacific basin (120°E–80°W), and (c) Atlantic basin (80°W–30°E) from CGCM/SSiB. (bottom) Also shown here are the differences of the annual mean of zonal-mean current speed (cm s^{-1}) between CGCM/SSiB and CGCM/SLS (SSiB − SLS). Values where differences are statistically significant at the 95% confidence level are color shaded.

as the model fails to capture the coastal upwelling and low-level clouds. Overall, the simulation with SSiB is more successful than the one with SLS. The situations are very different from the observation in the equatorial Atlantic, where the zonal SST gradient in the two CGCM has a different sign than in the observation in most of the basin. Such an unrealistic feature is common to most GCM simulations in the CMIP3 (Lin 2007; Richter and Xie 2008) or CMIP5 archives. The reasons for the comparatively poorer performance of CGCMs in the Atlantic are still unclear at the present time.

Figure 10 gives a view of the upper-ocean structure (temperature and zonal current speed) along the equatorial Pacific (2°S–2°N) simulated by CGCM/SLS and CGCM/SSiB. In the observation (not shown), the thermocline is deeper in the western Pacific and shallower in the east, with a slope that balances the easterly wind stress along the equator. Both simulations capture this configuration of the mixed layer and thermocline. Compared to CGCM/SLS,

the thermocline depth in CGCM/SSiB is shallower in the west between 120°E and 180° and deeper in the east between 120° and 80°W. The reduced tilt is consistent with the weakened surface easterly wind stress, zonal current speed, and the warming in the SST along the equator, as well as the weaker and shallower core of the equatorial under current (also indicated in Fig. 8). The deepening of the thermocline in the eastern Pacific in the CGCM/SSiB also suggests a weakening of equatorial upwelling consistent with the eastern equatorial Pacific warming.

b. Seasonal cycle and interannual variability of tropical SST

The previous subsections demonstrate that land surface processes affect the CGCM simulation of the annual-mean climate in the tropical ocean basins. In this subsection we concentrate on the equatorial Pacific and show that the seasonal cycle and interannual variability of SST are also affected. Figure 11 displays the
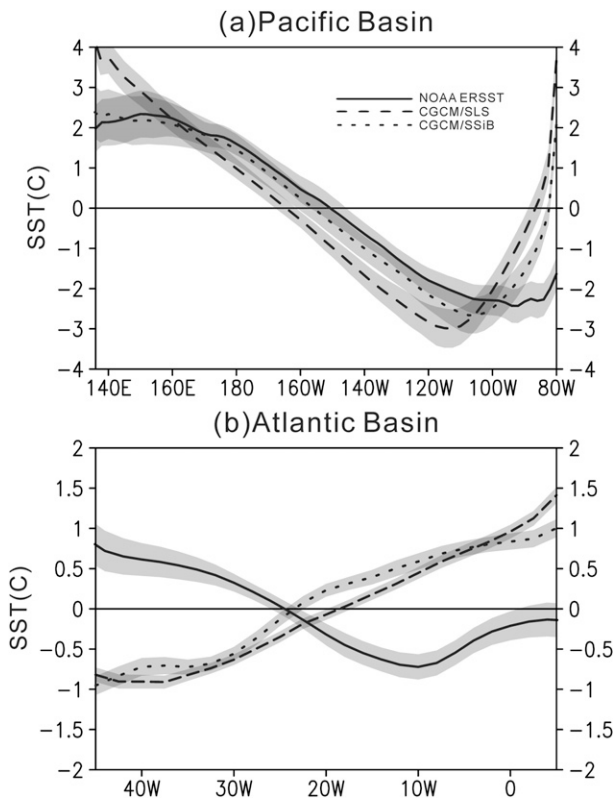
FIG. 9. Annual-mean SST deviation (°C) from the zonal mean for the (a) Pacific basin and (b) Atlantic basin, averaged along the equator over 2°S–2°N from Reynolds SST (solid curve), CGCM/SLS (dashed curve), and CGCM/SSiB (dotted curve). Shaded areas are their standard deviations.

FIG. 10. Annual-mean temperature profiles (°C; contours) and zonal current speed (cm s^{-1}; shaded) for the Pacific basin averaged over 2°S–2°N from (a) CGCM/SLS and (b) CGCM/SSiB. The contour interval is 1°C.

deviations from the annual mean of the monthly-mean SSTs along the equatorial Pacific (2°S–2°N). The observation shows strong east–west asymmetry, with a dominance of the semiannual harmonic in the west and of the annual harmonic in the east. In this part of the ocean, the warm phase is in the first half of the year peaking in March, and the cold phase is in the second half of the year peaking in September at about 100°W. The warm phase is stronger than the cold phase, and the two phases exhibit a clear westward propagation. The seasonal cycle of SSTs is better simulated in CGCM/SSiB with superior amplitude and phases in the eastern Pacific and better westward propagation characteristics comparing to CGCM/SLS. The peak months of warm and cold phases of CGCM/SLS (Fig. 11d) show a 2- and 3-month delay compared to the observation, respectively.

The leading mode of interannual variability in the tropical Pacific is ENSO. ENSO events tend to reach their maximum SST anomalies toward the end of the calendar year (e.g., Xiao and Mechoso 2009a,b). The occurrence of such a locking agrees with the seasonal variations in ocean–atmosphere coupling strength (e.g.,
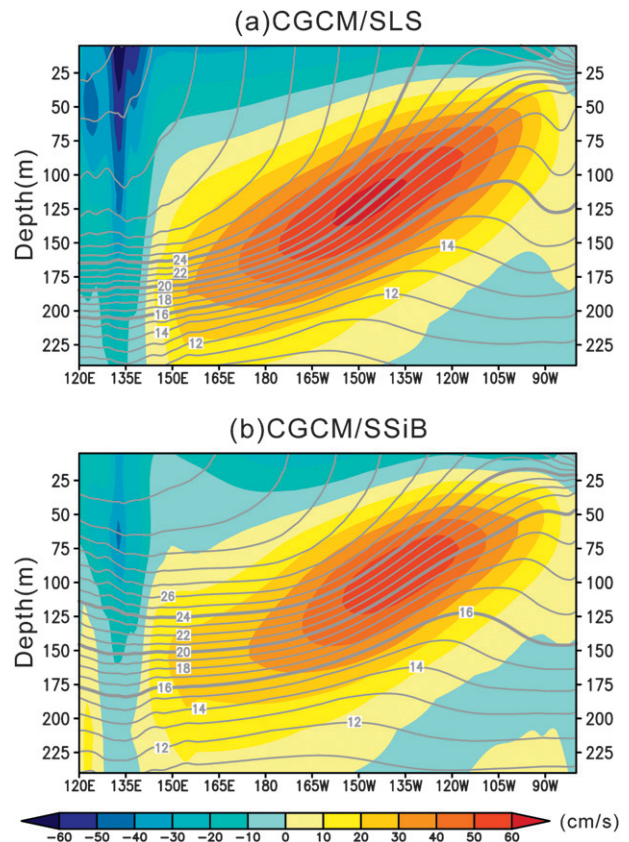
Philander et al. 1984; Philander 1985). Figure 12 shows the seasonal variance of the Niño-3 indices from the observation (NOAA ERSST) and the two CGCM simulations. The NOAA ERSST shows large variances toward the end of the calendar year. This feature is missed by CGCM/SLS, in which larger variances are in the northern summer. The feature is captured by CGCM/SSiB, albeit with too high variance values during the northern winter. The more realistic seasonal variance in SST obtained in CGCM/SSiB in the equatorial Pacific is consistent with the better seasonal cycle and interannual variability (e.g., Mechoso et al. 2003).

Several hypotheses on the reasons for the seasonal phase locking have been proposed and tested in intermediate-complexity models (e.g., Tziperman et al. 1997, 1998; Neelin et al. 2000) or CGCM studies (e.g., Xiao and Mechoso 2009a,b). Xiao and Mechoso (2009a,b) support the validity of two proposed mechanisms for such a phase lock: 1) the seasonal warming of the cold tongue early in the calendar year (January–April) favors the initial growth of an event, and 2) the warm surface waters returning in the western basin from the
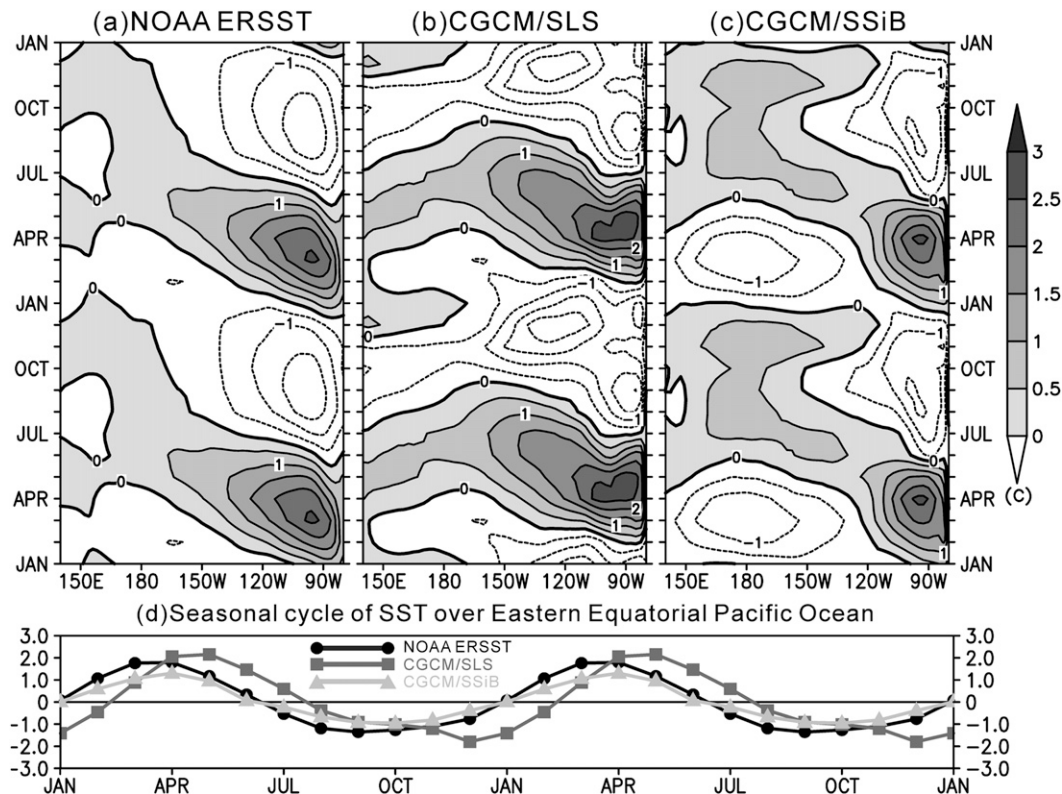
FIG. 11. Seasonal cycle of equatorial SST (°C; 2°S–2°N) in terms of deviations from the annual mean for the Pacific Basin from (a) Reynolds SST, (b) CGCM/SLS, and (c) CGCM/SSiB. (d)The seasonal cycles of SST deviations averaged over (2°–2°S, 130°–80°W).

Northern Hemisphere to the Southern Hemisphere toward the end of the calendar year (November–January) favor the demise of ongoing events. Both CGCM experiments show the seasonal warming of the eastern equatorial Pacific cold tongue early in the calendar year (not shown here). The conditions for the second mechanism to act, however, are only present in CGCM/SSiB. Figure 13 shows the seasonal migration of warm surface waters indicated by SST deviation in reference to the domain annual mean (15°S–15°N, 150°E–170°W), as well as convergence zones indicated by precipitation. According to the observation, warm SST anomalies propagate southward across the equator beginning at around September–February. Displacements in strong convection also follow the propagation of warm SST anomalies. Such a feature is captured by CGCM/SSiB and missed by CGCM/SLS. The reason for no southward migration in CGCM/SLS is the too strong equatorial cold tongue all year round as indicated by cold SST anomalies and little precipitation between ±5°. As shown in Fig. 7, in the CGCM/SSiB the equatorial easterly trades are weaker, resulting in a warmer and more realistic climate mean state in zonal SST gradient and thermocline structure along the equator. A better warm pool–cold tongue

structure also favors the work of coupled feedback processes, in such a way that the equatorial seasonal cycle of SST is improved (Fig. 11). The better westward propagation of warm anomalies over the central and
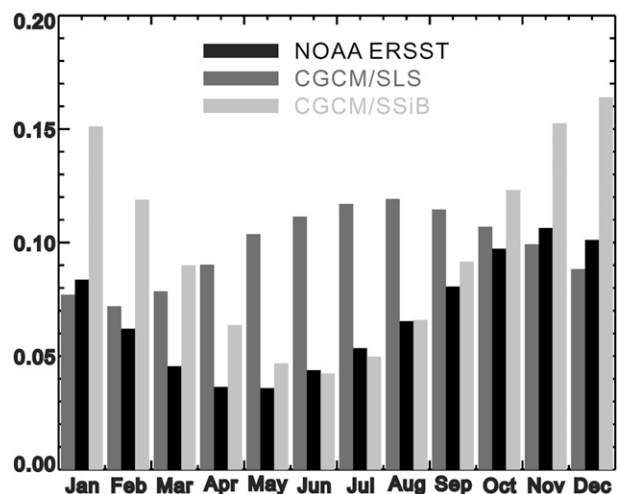

FIG. 12. Seasonal variance of the Niño-3 indices from NOAA ERSST, CGCM/SLS, and CGCM/SSiB. The analysis period for NOAA ERSST covers from 1901 to 2000, and the period for CGCM/SLS and CGCM/SSiB is from 100-year-long simulations.
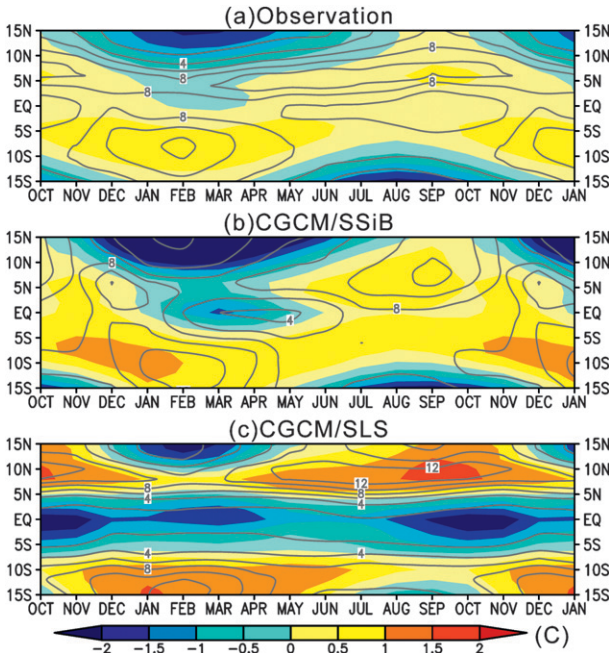
FIG. 13. Seasonal migration of warm surface waters indicated by SST deviation in reference to the domain annual average (°C; contours) and of convergence zones indicated by precipitation (mm day^{-1}; shading), in the western basin (averaged between 150°E and 170°W) from (a) CMAP precipitation and NOAA ERSST, (b) CGCM/SSiB, and (c) CGCM/SLS.

western Pacific could also be another reason for the better ENSO phase locking as the propagation of warm anomalies during the second half of the calendar year over the central Pacific. In CGCM/SLS, there is no westward propagation over the date line, and the cold anomalies disfavor an ongoing El Niño event. Therefore, the SST variance is largest in August and starts to decay afterward.

Figure 14 shows the power spectrum of Niño-3 indices from NOAA ERSST, CGCM/SLS, and CGCM/SSiB. The spectrum analysis was performed using the MATLAB

software with FFT spectrum function and the window width set to 512 (with a total 1200 monthly-mean SST fields for both observation and simulations). The NOAA ERSST shows two major significant (above 95% level of significance) peaks at around 6 and 4 yr on interannual time scales. The CGCM/SLS shows a dominant peak at around 8 yr and another weaker peak at around 3 yr. The CGCM/SSiB shows two major peaks at around 7 and 4 yr, which are very close to the NOAA ERSST in terms of frequency and power.

c. The indirect effect of land surface processes due to ocean–atmosphere interactions

The results from the above subsections show that ocean–atmosphere interactions contribute to the sensitivity of simulated global climate to the representation of land surface processes. To quantify such an indirect effect, we introduce a parameter Γ_I defined in the following way:

$$\Gamma_I \equiv \frac{100|\delta_C - \delta_A|}{\max\limits_{x,y}(|\delta_C - \delta_A|)}, \qquad (2)$$

where δ_C and δ_A are the CGCM and AGCM sensitivities (SSiB minus SLS) of a physical quantity, respectively. Larger values of Γ_I, therefore, indicate strong feedbacks from the oceanic perturbations.

Figure 15 displays the distributions of Γ_I for surface air temperature, precipitation, and total cloud cover. Figure 15 also indicates the maximum value of $|\delta_C - \delta_A|$ for each field. All these three fields show very large values of Γ_I over ocean especially over the Pacific since SSTs are active in the coupled runs. Interestingly, the generally nonzero values of Γ_I over land indicates the indirect effect of land surface processes from the remote impact of the oceanic perturbations originated from the direct impact of land–atmosphere interactions.
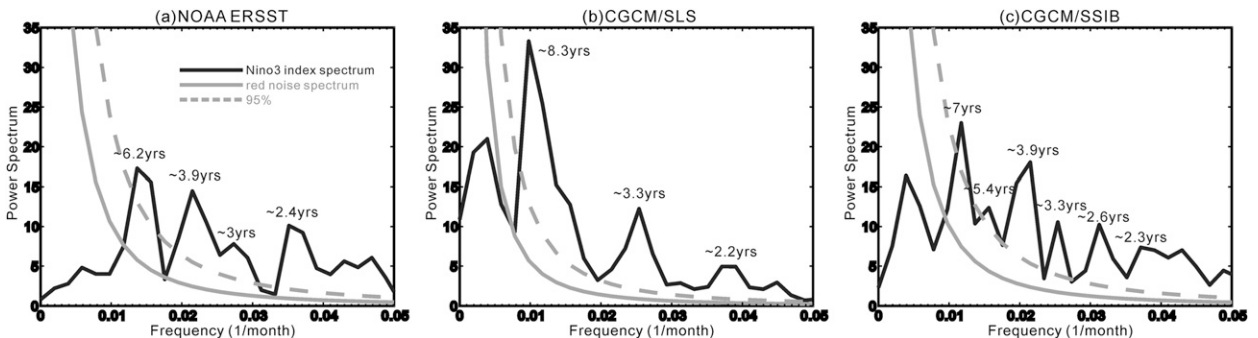

FIG. 14. Power spectra of the Niño-3 index (black curves) from (a) NOAA ERSST for the period of 1901–2000 and from (b) CGCM/SLS and (c) CGCM/SSiB for 100-year-long simulations. Also shown in (a)–(c) are the red-noise spectra (gray curves) and their 95% level of significance (dashed gray curves) based on the lag-1 autocorrelation.
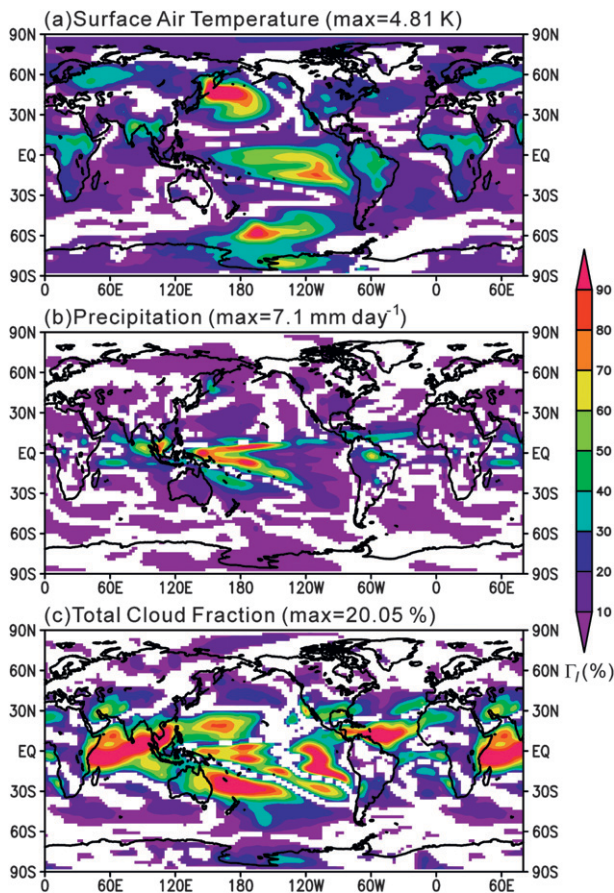
FIG. 15. Indirect effect of land surface processes on annual-mean (a) surface air temperature, (b) precipitation, and (c) total cloud cover calculated from the experiments of CGCM/SSiB, CGCM/SLS, AGCM/SSiB, and AGCM/SLS based on Eq. (2): $\Gamma_I \equiv 100|\delta_C - \delta_A|/\max_{x,y}(|\delta_C - \delta_A|)$. See the text for more information. Regions where differences are statistically significant at the 95% confidence level are color shaded.

For surface air temperature (Fig. 15a), the indirect effect almost affects the entire globe as indicated by large values of Γ_I. The largest signals are over the eastern Pacific extending toward the western Pacific warm pool and the northern and southern oceans. These larger values are mainly connected to the sensitivity of surface wind stress, cloud cover, and associated sensitivities in mean zonal SST gradient. Over land, large values of Γ_I on the average of 30%–60% (1.44–2.89 K) are also present in northern South America, southern and southeastern Asia, northern Eurasia, eastern and southern United States, tropical Africa, and part of Antarctica.

For the indirect effect on precipitation (Fig. 15b), we find region of largest sensitivity to be over the tropical Pacific, especially over the western Pacific warm pool and SPCZ. This is closely linked to the sensitivity in SSTs. Large indirect effect of precipitation is also found

over the ITCZs in the Atlantic and Indian Oceans. The values of Γ_I in precipitation over land are generally smaller compared to those in surface air temperature. Nevertheless, we still find Γ_I to be ~(10%–40%) (0.71–2.84 mm day^{-1}) over tropical South America, tropical Africa, central and eastern United States, Australia, and the Maritime Continent. For the indirect effect of total cloud cover (Fig. 15c), the larger values of Γ_I are over the tropical oceans in association to changes in convection, except for the large values over the eastern Pacific Ocean associated with the sensitivity of stratocumulus clouds. There are large values over the northern and southern Pacific associated with variations in the storm tracks.

The fields we presented here show large indirect effect over both ocean and land. This suggests that ocean–atmosphere interactions further modified the direct impact of land surface processes on the global-mean climate. The effect also impacts regions over the so-called hot spots [~(1–3) mm day^{-1} in precipitation]. The magnitude of such indirect effect is therefore strong enough to suggest that comprehensive studies on the importance of land surface processes on the global climate have to be made in a system that allows for atmosphere–ocean interactions.

4. Summary and conclusions

We have examined the sensitivity of global climate and its variability to land surface processes in a coupled ocean–atmosphere system. The emphasis was on the interactive soil moisture and vegetation biophysical processes. Our approach was based on simulations by the UCLA AGCM either uncoupled (i.e., with prescribed SSTs) or coupled to the MIT OGCM. Two configurations of land surface schemes in the AGCM were considered: 1) a simple representation of land surface processes (SLS), which specifies albedo and soil moisture availability, and 2) the Simplified Simple Biosphere Model (SSiB), which allows for interactive soil moisture and vegetation biophysical processes. In the AGCM, the atmospheric composition (CO_2 and other trace gases) remained constant throughout the experiments. Here, we defined the sensitivity as the differences of annual-mean state between SSiB and SLS fields (SSiB minus SLS). Several observational datasets are also employed to assess the extent to which results are realistic.

Our results from both AGCM and CGCM simulations demonstrate significant atmospheric sensitivity in the annual means of surface air temperature, precipitation, clouds, and large-scale circulation over both land and ocean. Over the oceans, the CGCM sensitivities are more significant than AGCM, especially in the Pacific

basin since the SST is prescribed in the AGCM simulations and the ocean–atmosphere interactions are hampered. The sensitivity also extends to the oceanic mean state in the coupled runs. The annual means of wind driven currents, zonal SST gradient, and thermocline structures along the equatorial Pacific are also changed and more realistic in the CGCM simulations with SSiB.

In addition to oceanic mean state, land surface processes also have a significant influence on the seasonal cycle and interannual variability of SSTs in the eastern equatorial Pacific. The seasonal cycle of SST has more realistic amplitudes and phase in the eastern Pacific and westward propagation characteristics in the coupled simulations with SSiB. The sensitivity also extends to ENSO frequency, magnitude, and peak timing in the annual cycle. The improvement of seasonal cycle and interannual variability of SSTs in the simulations with SSiB is likely due to a better tropical Pacific mean state modified by a better equatorial easterly trades, which favors the strong ocean–atmosphere coupled feedbacks over the equatorial Pacific. Based on our analyses, we further concluded that the weaker but more realistic easterly trades in the equatorial Pacific modified by the weaker convection over tropical land due to larger Bowen ratios are the key mechanisms to the sensitivities in the oceanic mean state, seasonal cycles, and interannual variability.

Our results further demonstrated that the oceanic perturbations due to land surface processes through ocean–atmosphere interactions can also feed back to the simulated global climate. To identify such an "indirect effect" of land surface processes, we introduce a nondimensional sensitivity parameter [Γ_I; Eq. (2)]. We computed and discussed the values of this parameter for surface air temperature, precipitation, and total cloud cover. All these three fields show very large values of Γ_I over ocean since SSTs are active in the coupled runs, and the sensitivity is generally small in the uncoupled runs. Most importantly, the generally nonzero values of Γ_I over land on the average of 10%–60% (1.44–2.89 K for surface air temperature and 0.71–2.84 mm day^{-1} for precipitation) indicates the indirect effect of land surface process from the remote impact of the oceanic perturbations originated from the direct impact of land–atmosphere interactions. This suggests that ocean–atmosphere interactions further modified the direct impact of land surface processes on the global-mean climate. The effect also impacts regions over the so-called hot spots [$\sim$(1–3 mm) day^{-1} in precipitation]. The magnitude of such an indirect effect is therefore strong enough to suggest that comprehensive studies on the importance of land surface processes on the global climate have to be made in a system that allows for atmosphere–ocean interactions.

We obtained a more realistic tropical climate with SSiB including a reduced double-ITCZ bias, better warm pool and cold tongue structure, more realistic seasonal cycles of SST in phases and amplitude, and better ENSO frequency and phase. Interestingly, little change or improvement was obtained over the Atlantic basin, including the subtropical highs, Namibian stratocumulus, and zonal SST gradient along the equator. Different from the results in Pacific, the CGCM and AGCM sensitivities over the Atlantic are generally similar (Fig. 2). Richter et al. (2012) using a CGCM suggested that either stronger convection in tropical South America or weaker convection in tropical Africa due to changes in the land surface conditions can result in stronger equatorial easterly trades in the Atlantic, which enhances equatorial upwelling and reduces the warm SST biases. In our case, convection in both tropical regions is weaker and therefore changes in the Atlantic equatorial trades and zonal SST gradients are not significant. The SST biases in the tropical Atlantic as well as biased high precipitation south of equator over the eastern Pacific (the double-ITCZ issue) might affect the sensitivity of our simulations (e.g., section 3c). Further experiments with different CGCMs may be necessary to obtain robust sensitivity.

Last, as indicated by changes of vertical heating profiles and large sensitivity of total cloud fraction, the three-dimensional cloud structure associated with the changes in convection and low clouds due to land surface processes also suggests large uncertainty in determining the cloud feedback in the future projections of climate under global warming scenario, as well as uncertainties in the interannual and decadal predictions.

REFERENCES

Arakawa, A., 2000: A personal perspective of the early years of general circulation modeling at UCLA. *General Circulation*

Model Development: Past, Present, and Future: Proceedings of a Symposium in Honor of Professor Akio Arakawa, D. A. Randall, Ed., Academic Press, 1–65.

——, and W. H. Schubert, 1974: Interaction of a cumulus ensemble with the large-scale environment. Part I. *J. Atmos. Sci.,* **31,** 674–701.

Bader, D. C., C. Covey, W. J. Gutowski Jr., I. M. Held, K. E. Kunkel, R. L. Miller, R. T. Tokmakian, and M. H. Zhang, 2008: Climate models: An assessment of strengths and limitations. U.S. Climate Change Science Program and the Subcommittee on Global Change Research Department of Energy Office of Biological and Environmental Research Rep., 124 pp.

Barnett, T. P., L. Dumenil, U. Schlese, E. Roeckner, and M. Latif, 1989: The effect of Eurasian snow cover on regional and global climate variations. *J. Atmos. Sci.,* **46,** 661–685.

Betts, A. K., J. H. Ball, A. C. M. Beljaars, M. J. Miller, and P. Viterbo, 1996: The land-surface-atmosphere interaction: A review based on observational and global modeling perspectives. *J. Geophys. Res.,* **101,** 7209–7225.

Boone, A., and Coauthors, 2004: The Rhône-Aggregation Land Surface Scheme intercomparison project: An overview. *J. Climate,* **17,** 187–208.

Businger, J. A., J. C. Wyngaard, Y. Izumi, and E. G. Bradley, 1971: Flux–profile relationships in the atmospheric surface layer. *J. Atmos. Sci.,* **28,** 181–189.

Cazes-Boezio, G., D. Menemenlis, and C. R. Mechoso, 2008: Impact of ECCO ocean-state estimates on the initialization of seasonal climate forecasts. *J. Climate,* **21,** 1929–1947.

Deardorff, J. W., 1972: Parameterization of the planetary boundary layer for use in general circulation models. *Mon. Wea. Rev.,* **100,** 93–106.

Delworth, T. L., and S. Manabe, 1988: Influence of potential evaporation on the variabilities of simulated soil wetness and climate. *J. Climate,* **1,** 523–547.

——, and ——, 1989: The influence of soil wetness on near-surface atmosphere variability. *J. Climate,* **2,** 1447–1462.

Dorman, J. L., and P. Sellers, 1989: A global climatology of albedo, roughness length and stomatal resistance for atmospheric general circulation models as represented by the Simple Biosphere Model (SiB). *J. Appl. Meteor.,* **28,** 833–855.

Fu, X., and B. Wang, 2003: Influences of continental monsoons and air–sea coupling on the climate of the equatorial Pacific. *J. Climate,* **16,** 3132–3152.

Gent, P. R., and J. C. McWilliams, 1990: Isopycnal mixing in ocean circulation models. *J. Phys. Oceanogr.,* **20,** 150–155.

Gill, A. E., 1980: Some simple solutions for heat-induced tropical circulation. *Quart. J. Roy. Meteor. Soc.,* **106,** 447–462.

Harshvardhan, R. Davies, D. A. Randall, and T. G. Corsetti, 1987: A fast radiation parameterization for atmospheric circulation models. *J. Geophys. Res.,* **92,** 1009–1016.

——, ——, ——, ——, and D. A. Dazlich, 1989: Earth radiation budget and cloudiness simulations with a general circulation model. *J. Atmos. Sci.,* **46,** 1922–1942.

Henderson-Sellers, A., P. Irannejad, K. McGuffie, and A. J. Pitman, 2003: Predicting land-surface climates—Better skill or moving targets? *Geophys. Res. Lett.,* **30,** 1777, doi:10.1029/2003GL017387.

Hu, Z.-Z., E. K. Schneider, U. S. Bhatt, and B. P. Kirtman, 2004: Potential mechanism for response of El Niño–Southern Oscillation variability to change in land surface energy budget. *J. Geophys. Res.,* **109,** D21113, doi:10.1029/2004JD004771.

Köhler, M., 1999: Explicit prediction of ice clouds in general circulation models. Ph.D. dissertation, University of California, Los Angeles, 167 pp.

Koster, R. D., and Coauthors, 2004: Regions of strong coupling between soil moisture and precipitation. *Science,* **305,** 1138–1140, doi:10.1126/science.1100217.

——, and Coauthors, 2006: GLACE: The Global Land–Atmosphere Coupling Experiment. Part I: Overview. *J. Hydrometeor.,* **7,** 590–610.

Large, W. G., J. C. McWilliams, and S. Doney, 1994: Oceanic vertical mixing: A review and a model with a nonlocal boundary layer parameterization. *Rev. Geophys.,* **32,** 363–403.

——, G. Danabasoglu, S. C. Doney, and J. C. McWilliams, 1997: Sensitivity to surface forcing and boundary layer mixing in a global ocean model: Annual-mean climatology. *J. Phys. Oceanogr.,* **27,** 2418–2447.

Li, J.-L., M. Köhler, J. D. Farrara, and C. R. Mechoso, 2002: The impact of stratocumulus cloud radiative properties on surface heat fluxes simulated with a general circulation model. *Mon. Wea. Rev.,* **130,** 1433–1441.

Lin, J.-L., 2007: The double-ITCZ problem in IPCC AR4 coupled GCMs: Ocean–atmosphere feedback analysis. *J. Climate,* **20,** 4497–4525.

Lindzen, R. S., and S. Nigam, 1987: On the role of sea surface temperature gradients in forcing low-level winds and convergence in the tropics. *J. Atmos. Sci.,* **44,** 2418–2436.

Ma, H.-Y., C. R. Mechoso, Y. Xue, H. Xiao, C.-M. Wu, J.-L. Li, and F. De Sales, 2010: Impact of land surface processes on the South American warm season climate. *Climate Dyn.,* **37,** 187–203, doi:10.1007/s00382-010-0813-3.

——, X. Ji, J. D. Neelin, and C. R. Mechoso, 2011: Mechanisms for precipitation variability of the eastern Brazil/SACZ convective margin. *J. Climate,* **24,** 3445–3456.

——, M. Köhler, J.-L. F. Li, J. Farrara, C. R. Mechoso, R. Forbes, and D. E. Waliser, 2012: Evaluation of an ice cloud parameterization based on a dynamical-microphysical lifetime concept using CloudSat observations and the ERA-Interim reanalysis. *J. Geophys. Res.,* **117,** D05210, doi:10.1029/2011JD016275.

Marshall, J., A. Adcroft, C. Hill, L. Perelman, and C. Heisey, 1997: A finite-volume, incompressible Navier-Stokes model for studies of the ocean on parallel computers. *J. Geophys. Res.,* **102** (C3), 5753–5766.

Mechoso, C. R., and Coauthors, 1995: The seasonal cycle over the tropical Pacific in coupled ocean–atmosphere general circulation models. *Mon. Wea. Rev.,* **123,** 2825–2838.

——, J.-Y. Yu, and A. Arakawa, 2000: A coupled GCM pilgrimage: From climate catastrophe to ENSO simulations. *General Circulation Model Development: Past, Present and Future: Proceedings of a Symposium in Honor of Professor Akio Arakawa,* D. A. Randall, Ed., Academic Press, 539–575.

——, J. D. Neelin, and J.-Y. Yu, 2003: Testing simple models of ENSO. *J. Atmos. Sci.,* **60,** 305–318.

Meehl, G. A., 1994: Influence of the land surface in the Asian summer monsoon: External conditions versus internal feedbacks. *J. Climate,* **7,** 1033–1049.

Misra, V., 2008: Coupled interactions of the monsoons. *Geophys. Res. Lett.,* **35,** L12705, doi:10.1029/2008GL033562.

Neelin, J. D., F.-F. Jin, and H.-H. Syu, 2000: Variations in ENSO phase locking. *J. Climate,* **13,** 2570–2590.

Pan, D.-M., and D. A. Randall, 1998: A cumulus parameterization with a prognostic closure. *Quart. J. Roy. Meteor. Soc.,* **124,** 949–981.

Paulson, C. A., 1970: Mathematical representation of wind speed and temperature profiles in the unstable atmospheric surface layer. *J. Appl. Meteor.,* **9,** 857–861.

Philander, S. G. H., 1985: El Niño and La Niña. *J. Atmos. Sci.,* **42,** 2652–2662.

——, T. Yamagata, and R. Pacanowski, 1984: Unstable air–sea interactions in the tropics. *J. Atmos. Sci.,* **41,** 604–613.

Redi, M. H., 1982: Oceanic isopycnal mixing by coordinate rotation. *J. Phys. Oceanogr.,* **12,** 1154–1158.

Reynolds, R. W., and T. M. Smith, 1995: A high-resolution global sea surface temperature climatology. *J. Climate,* **8,** 1571–1583.

Richter, I., and S.-P. Xie, 2008: On the origin of equatorial Atlantic biases in coupled general circulation models. *Climate Dyn.,* **31,** 587–598.

——, ——, A. T. Wittenberg, and Y. Masumoto, 2012: Tropical Atlantic biases and their relation to surface wind stress and terrestrial precipitation. *Climate Dyn.,* **38,** 985–1001, doi:10. 1007/s00382-011-1038-9.

Rodwell, M. J., and B. J. Hoskins, 2001: Subtropical anticyclones and summer monsoons. *J. Climate,* **14,** 3192–3211.

Sellers, P. J., Y. Mintz, Y. C. Sud, and A. Dalcher, 1986: A simple biosphere model (SiB) for use within general circulation models. *J. Atmos. Sci.,* **43,** 505–531.

Seneviratne, S. I., D. Lüthi, M. Litschi, and C. Schär, 2006: Land-atmosphere coupling and climate change in Europe. *Nature,* **443,** 205–209.

Smith, T. M., R. W. Reynolds, T. C. Peterson, and J. Lawrimore, 2008: Improvements to NOAA's historical merged land–ocean surface temperature analysis (1880–2006). *J. Climate,* **21,** 2283–2296.

Solomon, S., D. Qin, M. Manning, M. Marquis, K. Averyt, M. M. B. Tignor, H. L. Miller Jr., and Z. Chen, Eds., 2007: *Climate Change 2007: The Physical Science Basis.* Cambridge University Press, 996 pp.

Suarez, M. J., A. Arakawa, and D. A. Randall, 1983: The parameterization of the planetary boundary layer in the UCLA general circulation model: Formulation and results. *Mon. Wea. Rev.,* **111,** 2224–2243.

Swann, A. L. S., I. Y. Fung, and J. C. H. Chiang, 2011: Mid-latitude afforestation shifts general circulation and tropical precipitation. *Proc. Natl. Acad. Sci. USA,* **109,** 712–716.

Tziperman, E., S. E. Zebiak, and M. A. Cane, 1997: Mechanisms of seasonal–ENSO interaction. *J. Atmos. Sci.,* **54,** 61–71.

——, M. A. Cane, S. E. Zebiak, Y. Xue, and B. Blumenthal, 1998: Locking of El Niño's peak time to the end of the calendar year in the delayed oscillator picture of ENSO. *J. Climate,* **11,** 2191–2199.

Wang, B., Q. Ding, X. Fu, I.-S. Kang, K. Jin, J. Shukla, and F. Doblas-Reyes, 2005: Fundamental challenge in simulation and prediction of summer monsoon rainfall. *Geophys. Res. Lett.,* **32,** L15711, doi:10.1029/2005GL022734.

Wei, J., and P. A. Dirmeyer, 2010: Toward understanding the large-scale land-atmosphere coupling in the models: Roles of different processes. *Geophys. Res. Lett.,* **37,** L19707, doi:10.1029/ 2010GL044769.

——, ——, and J. Zhang, 2010: Land-caused uncertainties in climate change simulations: A study with the COLA AGCM. *Quart. J. Roy. Meteor. Soc.,* **136,** 819–824.

Wilks, D. S., 2006: *Statistical Methods in the Atmospheric Sciences.* 2nd ed. International Geophysical Series, Vol. 91, Academic Press, 627 pp.

Wu, R., B. P. Kirtman, and K. Pegion, 2006: Local air–sea relationship in observations and model simulations. *J. Climate,* **19,** 4914–4932.

Xiao, H., and C. R. Mechoso, 2009a: Correlative evolutions of ENSO and the seasonal cycle. *J. Atmos. Sci.,* **66,** 1041–1049.

——, and ——, 2009b: Seasonal cycle–El Niño relationship: Validation of hypotheses. *J. Atmos. Sci.,* **66,** 1633–1653.

Xie, P., and P. A. Arkin, 1997: Global precipitation: A 17-year monthly analysis based on gauge observations, satellite estimates, and numerical model outputs. *Bull. Amer. Meteor. Soc.,* **78,** 2539–2558.

Xue, Y., 1997: Biosphere feedback on regional climate in tropical North Africa. *Quart. J. Roy. Meteor. Soc.,* **123B,** 1483–1515.

——, P. J. Sellers, J. L. Kinter III, and J. Shukla, 1991: A simplified biosphere model for global climate studies. *J. Climate,* **4,** 345–364.

——, H. G. Bastable, P. A. Dirmeyer, and P. J. Sellers, 1996a: Sensitivity of simulated surface fluxes to changes in land surface parameterizations—A study using ABRACOS data. *J. Appl. Meteor.,* **35,** 386–400.

——, M. J. Fennessy, and P. J. Sellers, 1996b: Impact of vegetation properties on U.S. summer weather prediction. *J. Geophys. Res.,* **101** (D3), 7419–7430.

——, F. De Sales, W. Li, C. R. Mechoso, C. Nobre, and H.-M. H. Juang, 2006: Role of land surface processes in South American monsoon development. *J. Climate,* **19,** 741–762.

——, ——, R. Vasic, C. R. Mechoso, S. D. Prince, and A. Arakawa, 2010: Global and seasonal assessment of interactions between climate and vegetation biophysical processes: A GCM study with different land–vegetation representations. *J. Climate,* **23,** 1411–1433.

Zeng, N., and J. D. Neelin, 1999: A land–atmosphere interaction theory for the tropical deforestation problem. *J. Climate,* **12,** 857–872.

——, R. E. Dickinson, and X. Zeng, 1996: Climatic impact of Amazon deforestation—A mechanistic model study. *J. Climate,* **9,** 859–883.